ChemCatChem

Research Article
doi.org/10.1002/cctc.202500156

Chemistry Europe
European Chemical Societies Publishing

www.chemcatchem.org

Copper-Based Nitrides Outperform Phosphides in Nitrate Electroreduction to Ammonia: The Cooperative Role of the Cu_3N/CuO Interface

Paz Stein,[a] Henry Hall,[a, b] Ran Shimoni,[a] Noam E. Amitay,[a] Dyuti Bandyopadhyay,[a] Alevtina Neyman,[a] Ronen Bar-Ziv,*[c] and Maya Bar Sadan*[a]

Binary compounds consisting of Cu(I) and moderately electronegative elements (N, P) are attractive semiconductors for optoelectronic and electrocatalytic applications. This study investigates the electrochemical reduction of nitrate to ammonia (NO_3RR) using copper-based catalysts, specifically Cu_3N and Cu_3P. Inhibiting the competitive hydrogen evolution reaction and ensuring active hydrogen (H*) for NH_3 production during NO_3RR pose significant challenges. Our research demonstrates that while Cu_3P is effective in the initial reduction of nitrate to nitrite, it fails to produce NH_3 at more negative potentials due to competition with the hydrogen evolution reaction (HER). In contrast, Cu_3N exhibits remarkable performance, achieving an ammonia yield rate of 48.8 mmol h^{-1} $mmol^{-1}_{cat}$ at −0.9 V_{RHE}, accompanied by considerable Faradaic efficiency and durability. The formation of a Cu_3N/CuO interface during the catalysis is crucial for its activity, facilitating efficient NO_3RR through a stepwise reduction mechanism. The study provides insights into the surface modifications and mechanistic aspects of these catalysts during NO_3RR, offering guidance for strategically developing more efficient catalysts for nitrate reduction to ammonia.

1. Introduction

The increasing drive for clean energy technologies relies significantly on the availability of efficient, cost-effective, and abundant materials for catalyzing various reactions. A considerable emphasis has been placed on decarbonizing the production of chemicals and fuels. Renewable energy resources are acknowledged as promising sources to meet current energy demands without environmental repercussions. Among these resources, green fuels have garnered significant attention due to their environmentally friendly attributes and considerations for human health. Hydrogen and ammonia stand out as key candidates for future green fuels, holding crucial roles in achieving a net-zero carbon economy due to their absence of carbon emissions at the point of use.[1] Notably, in recent years, there has been a growing interest in electrochemical ammonia production as a replacement for the energy-intensive Haber–Bosch process.[1–3]

While sustainable fuels show promise in laboratory settings, their large-scale commercial implementation is in early development. The electrochemical nitrate reduction reaction (NO_3RR: $NO_3^- + 8e^- + 6H_2O \rightarrow NH_3 + 9OH^-$) garners attention due to the weak N═O bond (204 kJ mol^{-1}), high solubility in aqueous electrolytes, and widespread availability of nitrate.[3] As a common environmental pollutant from industrial wastewater, liquid nuclear waste, and agricultural runoff; nitrate requires careful consideration.[4] An ammonia-selective electrochemical NO_3RR offers an eco-friendly alternative for both ammonia synthesis and freshwater treatment, concurrently achieving dual objectives of pollutant elimination and green chemical production.[5]

Nitrate electroreduction is a proton-coupled electron process (PCET), where electrons act as the reductant and protons as the hydrogenation agent. *NO (*indicates adsorbed species on the catalyst) is a key intermediate in steering the selectivity of nitrate reduction.[6] If *NO is hydrogenated into *HNO, the main product will be NH_3, whereas other reaction pathways lead to N_2.[7] During NO_3RR, hydrogen evolution reaction, HER, ($2H^+ + 2e^- \rightarrow 2{*}H \rightarrow H_2$) occurs concurrently as an unavoidable parasitic reaction. To increase the Faradic efficiency (FE) of NO_3RR, the HER should be suppressed. However, active hydrogen (*H) is indispensable in the successive hydrogenation steps to form NH_3 and therefore, a balance between *H supply and consumption should be carefully maintained. A deficient *H supply will decelerate ammonia production, whereas an excess of weak-bonded *H will cause dimerization of hydrogen atoms to produce H_2.[8]

[a] P. Stein, H. Hall, R. Shimoni, N. E. Amitay, D. Bandyopadhyay, A. Neyman, M. Bar Sadan
Department of Chemistry, Ben Gurion University, Beer-Sheva 8410501, Israel
E-mail: barsadan@bgu.ac.il

[b] H. Hall
Department of Chemistry, University of Oxford, Oxford OX1 4BH, UK

[c] R. Bar-Ziv
Department of Chemistry, Nuclear Research Center Negev, P.O. Box 9001, Beer-Sheva 84190, Israel
E-mail: bronen@post.bgu.ac.il

Supporting information for this article is available on the WWW under https://doi.org/10.1002/cctc.202500156

During electrocatalysis, changes to the oxidation state of the surface atoms of metallic catalysts are crucial for enhancing or altering their catalytic behavior. For example, the formation of NiOOH/Ni_3N interface on Ni_3N nanosheets significantly improved oxygen evolution reaction (OER) activity by increasing active site exposure and conductivity.[9] Similarly, in electrochemical CO_2 reduction, controlling copper oxidation states and morphology through electro-redeposition enhanced efficiency and selectivity toward methylene production, particularly due to Cu^+ formation at high overpotentials.[10] Given these insights, it is crucial to characterize catalysts during and after reactions to understand dynamic surface changes and their mechanistic implications.

Owing to their abundance, cost-effectiveness, and promising performances, Cu-based catalysts have drawn significant attention in the field of electrochemical nitrate reduction to ammonia, as many studies have been aiming to elucidate their specific roles and mechanisms in catalysis.[11–13] Among transition metals, Cu has the highest occupied molecular orbital (HOMO, d-orbital) and at the same time, the lowest unoccupied molecular orbital (LUMO); similar to that of nitrate (π-orbital). This allows Cu to efficiently inject electrons into the N—O bond of nitrate, thereby activating the NO_3RR process.[14] Various Cu-based catalysts, including Cu alloys,[15] Cu oxides,[16] and Cu single-atom catalysts,[17] have been investigated and have showed improved efficiencies.

Meanwhile, the introduction of nonmetal elements (such as N, P, or B) to construct Cu-based nanostructures has been rarely reported. However, this approach could significantly enhance their performance by strongly influencing the electronic configuration of Cu. While nitrides and phosphides of first-row non-noble transition metals have shown promise as electrocatalysts for CO_2 reduction and water splitting,[18–21] their potential for nitrate reduction to ammonia in alkaline/neutral conditions remains largely unexplored. The limited *H adsorption capacity on the catalyst often hinders the prompt hydrogenation of the surface-bound N-intermediates (NO* and so on.). Therefore, we introduce copper(I) phosphide (Cu_3P) and copper(I) nitride (Cu_3N) catalysts, which feature Cu and P or N centers with positive and negative charges respectively.[18,22] In this configuration, Cu serves as the nitrate-acceptor center, while P or N acts as the proton-acceptor center. This tailored surface composition and electronic structure can potentially address the challenges associated with $*NO_3$ and *H coverage.[15,23]

Our findings indicate that although Cu_3P is effective in the initial reduction of nitrate to nitrite, it fails to produce NH_3 at more negative potentials due to competition with the hydrogen evolution reaction (HER). In contrast, Cu_3N exhibits remarkable performance, achieving an ammonia yield of 48.8 mmol h^{-1} $mmol_{cat.}$ at -0.9 V_{RHE}, with high Faradaic efficiency. During NO_3RR, surface modifications occur, revealing a thin oxide layer interfacing with an underlying Cu_3N and facilitating efficient NO_3RR through a stepwise reduction mechanism. The observed differences in performance offer critical guidance for the strategic development of more efficient catalysts for nitrate reduction to ammonia.

2. Experimental Section

2.1. Synthesis of Cu_3N Nanocubes

Cu_3N NCs were synthesized by modifying a published method.[24] In a 50 mL three-necked round-bottom flask, 60 mg of $Cu(NO_3)_2{\cdot}3H_2O$ (0.24 mmol) was mixed with 7.5 mL of oleylamine and 2.5 mL of octadecene. The solution was purged with N_2 and subjected to vacuum cycles. The mixture was heated to 120 °C for 60 min under vacuum and then ramped to 240 °C at 10 °C/min. After maintaining 240 °C for 15 min, the flask was cooled to room temperature. Optimization of the synthesis as a function of temperature was tested as described in the Supporting Information. The product was washed with chloroform and ethanol, centrifuged at 12,000 rpm for 10 min (repeated 3 times), dried under vacuum, and stored under inert conditions.

2.2. Synthesis of Cu_3P Nanoparticles

In a 100 mL three-necked flask, 10 mmol of hexadecylamine and 25.34 mL of octadecene were heated to 50 °C under vacuum. After 30 min, 3 mL of triphenylphosphite was injected, followed by heating to 60 °C for 30 min. A solution of 1 mmol $CuCl_2$ in 2 mL ethanol was injected and the mixture was heated at 6 °C/min to 150 °C for 60 min under N_2. The temperature was further raised to 270 °C at 4 °C/min and held for 60 min before cooling to 30 °C. The product was washed with chloroform and isopropanol via centrifugation, dried under a vacuum, and stored in a glove box. For the ligand exchange process, the Cu_3P nanoparticles (25 mg) were sonicated in chloroform followed by the addition of formamide and hexafluorophosphoric acid. After phase separation, the upper layer was washed with ethanol, dried under vacuum, and stored in inert conditions.

2.3. Electrochemical Measurements

Working electrodes were prepared by dispersing the catalyst, carbon black, and Nafion to produce a homogeneous ink. The ink was drop-casted onto a polished glassy carbon electrode. The electrolyte was a 0.1 M phosphate buffer saline (PBS) for reference experiments and a 0.1 M PBS/$NaNO_3$ (pH 7.7) for the catalytic NO_3RR experiments, chosen to maintain a stable pH and avoid potential shifts due to pH changes during the reaction as well as to minimize NH_3 evaporation. In a typical H-cell, the compartments were separated with a Nafion membrane; the active material comprised the working electrode, the counter electrode was Pt, whereas Ag/AgCl in saturated KCl was the reference electrode. All the potentials refer to the reversible hydrogen electrode (RHE). For more details on the synthesis and electrochemical measurements and the electrochemical surface area (ECSA) measurements, see the Supporting Information.

3. Results and Discussion

3.1. Materials Characterization

Transmission electron microscopy (TEM) was used to study the morphology of the synthesized nanostructures. Cu_3N formed aggregated nanocubes with a uniform size distribution, averaging 30 ± 3 nm (Figure 1a). The synthesized Cu_3P formed aggregates of round nanoparticles with an average size of 45 ±

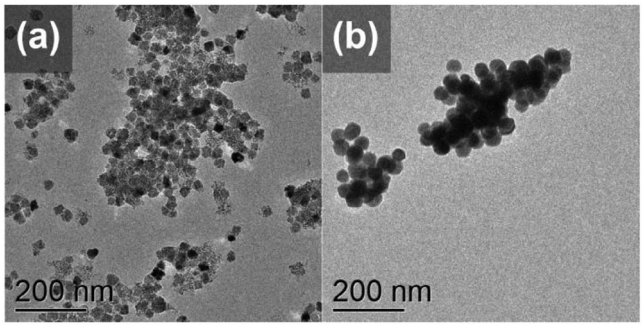

Figure 1. TEM images of (a) Cu_3N nanocubes and (b) Cu_3P nanoparticles.

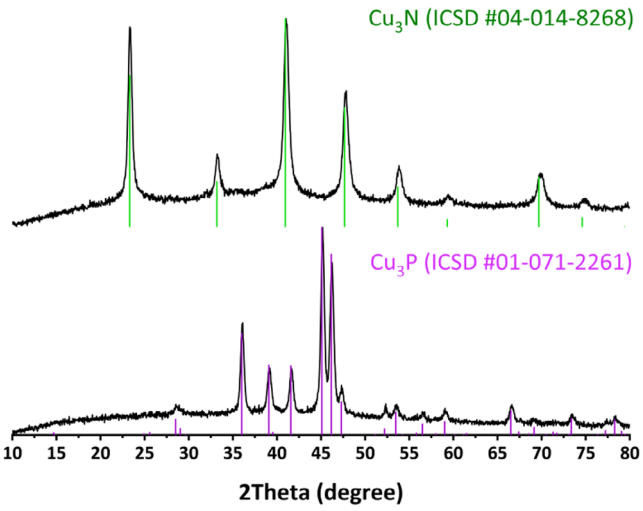

Figure 2. Powder X-ray diffraction patterns of the synthesized cubic Cu_3N, hexagonal Cu_3P, and their corresponding literature data.

5 nm (Figure 1b). SEM images of Cu_3N and Cu_3P are available in Figure S1a,b.

Powder X-ray diffraction (XRD) was used to identify and characterize the crystalline phases of the synthesized catalysts, as illustrated in Figure 2. The diffraction patterns confirmed that the Cu_3N and Cu_3P catalysts exhibited crystallographic phases, consistent with previously reported structures. The detailed lattice parameters for these phases are provided in Table S1.

X-ray photoelectron spectroscopy (XPS) was used to analyze the surface composition of the prepared catalysts. Detailed binding energy peak locations and associated oxidation states are provided in Table S2 in the Supporting Information. The Cu 2p spectrum in Figure 3 exhibits peaks corresponding to the different oxidation states of copper. The Cu_3N sample comprised a single oxidation state of Cu^+. The Cu_3P sample showed two main doublet pairs: the first, at lower binding energy, corresponds to an intermediate oxidation state (Cu^x, where $1 < x < 2$), indicative of both phosphide and oxide on the surface. At higher binding energy, the second doublet peak within the Cu_3P spectrum was attributed to copper atoms bound to phosphate species. Additionally, the analysis of Auger spectra in Figure S2 was performed to confirm the primary valence states, showing that Cu^+ was the predominant state for both catalysts. The analyzed spectra for N, P, and O are available in Figure S3a–c.

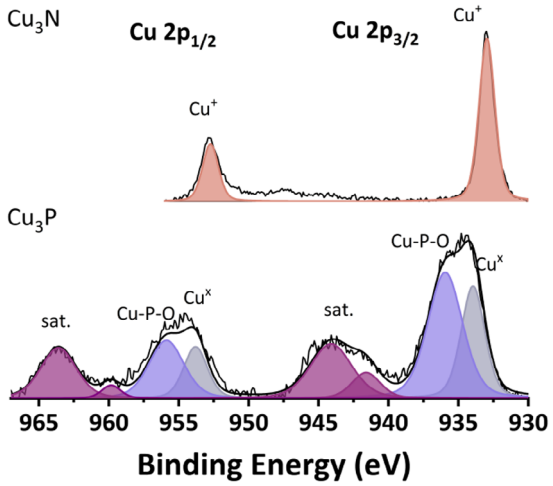

Figure 3. Cu2p spectra from the X-ray photoelectron analysis of the synthesized Cu_3N and Cu_3P catalysts.

3.2. NO_3RR Electrocatalytic Performance

The catalyst was mixed with carbon black (CB), deposited on a glassy carbon (GC) electrode with a loading of 0.5 mg cm^{-2} and evaluated for the NO_3RR in a typical H-type cell. Bare GC electrodes coated with CB were also tested under the same conditions for comparison. First, we investigated the Cu_3N as the primary focus to elucidate the role and contribution of metal-nitrogen bonding in the NO_3^- reduction reaction (NO_3RR). Preliminary experiments were performed in 0.1 M phosphate buffer saline (PBS) to achieve efficient reaction kinetics and selectivity. The optimized $NaNO_3$ concentration was determined to be 0.1 M, balancing selectivity and NH_3 production rate (see Figure S4). Further experiments were performed to optimize the synthesis protocol of the Cu_3N structures, concluding that synthesis at 240 °C produced the most efficient electrocatalysts (see discussion in the Supporting Information and Figures S5–S7). Figure 4a displays the linear scan voltammograms (LSV) of the Cu_3N nanoparticles in 0.1 M PBS solution, which showed enhanced electrocatalytic current density and shifted onset potential in the presence of NO_3^-. Chronoamperometric experiments were conducted across a potential range from −0.2 V to −1.0 V versus RHE (using 2.5 C per experiment) and the reduction products, including nitrite and ammonia, were quantified using colorimetric methods (see calculations and the calibration curves in Figures S8 and S9).[25] The Faradaic efficiencies (FE) for NH_3 and NO_2^- are shown in Figure 4b, whereas the NH_3 yield rates are illustrated in Figure 4c. Below a potential of −0.5 V versus RHE, only the intermediate NO_2^- is produced in consistent to the first reduction-reaction step of NO_3^- ($*NO_3^- + H_2O + 2e^- \rightarrow *NO_2^- + 2OH^-$). According to the proposed electron-mediated pathway, NH_3 production began at −0.5 V versus RHE by further reducing $*NO_2^-$ to *NO, *HNO, $*H_2NO$,$*NH_2OH$, and finally to NH_3.[26] As the potential was shifted negatively from −0.5 V versus RHE, the Faradaic efficiency (FE) for NO_2^- gradually declined. Simultaneously, a significant portion of the consumed electrons was utilized to produce the desired NH_3, reaching its peak efficiency at −0.9 V versus RHE (FE of 76%, yield rate of 48.8 mmol

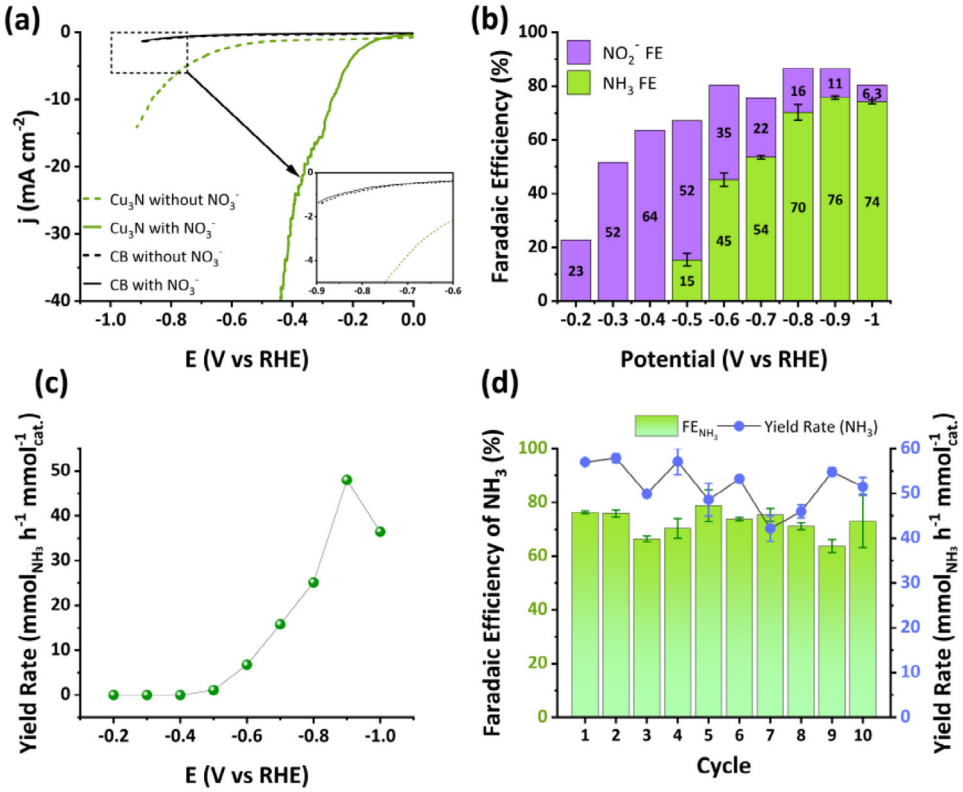

Figure 4. Electrochemical NO_3RR of Cu_3N nanocubes. (a) Linear scan voltammogram comparing Cu_3N catalysts and bare electrode with carbon black (CB) and Nafion in 0.1 M PBS, with and without 0.1 M $NaNO_3$. (b) Faradaic efficiencies for NH_3 and NO_2^-, measured over a potential range from −0.2 V to −1.0 V versus RHE. (c) NH_3 yield rates over a range from −0.2 V to −1.0 V versus RHE. (d) Faradaic efficiencies and yield rate of the stability testing of Cu_3N at −0.9 V versus RHE. All potentials are iR-corrected.

NH_3 per hour per mmol catalyst). In addition, the catalyst's stability was assessed continuously through repeated chronoamperometry at −0.9 V versus RHE over ten cycles, with 5 C applied per cycle and the electrolyte refreshed subsequently. Each cycle lasted approximately 30 min. The results in Figure 4d verified that Cu_3N maintained a consistent FE of the NO_3RR and ammonia yield rate, demonstrating its durability and effectiveness in continuous operations. To confirm the source of ammonia produced via electrochemical nitrate reduction, ^1H NMR spectroscopy was conducted using isotopically labeled nitrate sources.[27] The data presented in Figure S10 confirmed that the ammonium produced was solely derived from nitrate, as demonstrated by experiments conducted using both, $^{14}NO_3^-$ and $^{15}NO_3^-$, as the nitrogen sources.

While the catalytic activity of Cu_3N for NO_3RR was confirmed, it is vital to understand its surface modifications due to the catalytic reaction. The catalyst was loaded onto a carbon cloth electrode (2 mg on 1 × 1 cm^2) and subjected to passing a charge of 10 C at −0.9 V versus RHE, after which the catalyst was further characterized and analyzed. As shown in Figure S11, powder XRD analysis confirmed that Cu_3N maintained its cubic crystallographic phase. Surface analysis using XPS revealed the oxidized copper (CuO) and Cu_3N, as seen in the Cu 2p spectrum in Figure 5a and the N 1s spectrum in Figure S12. The peak positions and corresponding oxidation states are summarized in Table S3.

We have also investigated the effect of extended and prolonged catalytic usage on the Cu_3N surface and sublayer using XPS, specifically applying five cycles of 10 C chronoamperometry at −0.9 V versus RHE. The Cu 2p and N 1s spectra, as presented in Figure S13a,b, showed both copper oxide and nitride species. (Additional discussion is provided in the Supporting Information). The high-resolution TEM image in Figure 5b and its enlarged areas in Figure 5c,d, allowed for a close inspection of the comprising crystalline planes. The area shown in Figure 5c confirmed the presence of Cu_3N, specifically the (1 0 0) plane, whereas the magnified area in Figure 5d captured the presence of the (1 1 1) plane of CuO at the outer layer of the particle, with a thickness of ~4 nm. A representative TEM image at lower magnification, shown in Figure S14, revealed that the sharp-edged cubic particles have transformed into structures with rounder features. To conclude, during NO_3RR, surface modifications occur, revealing a thin, nanometer-thick oxide layer interfacing with an underlying Cu_3N substrate. In response to the observed surface oxidation of Cu_3N during nitrate reduction, CuO was selected as a reference material to evaluate the impact of a pre-existing oxidized state on catalytic performance. Detailed characterization of the CuO particles, including XRD, TEM, and XPS analyses (see Figure S15a–d in the Supporting Information), provides insights into their structural and surface properties. The electrochemical activity of the as-synthesized CuO revealed efficient conversion of nitrate to ammonia, 15.7 mmol NH_3 h^{-1} $mmol_{cat}^{-1}$, at

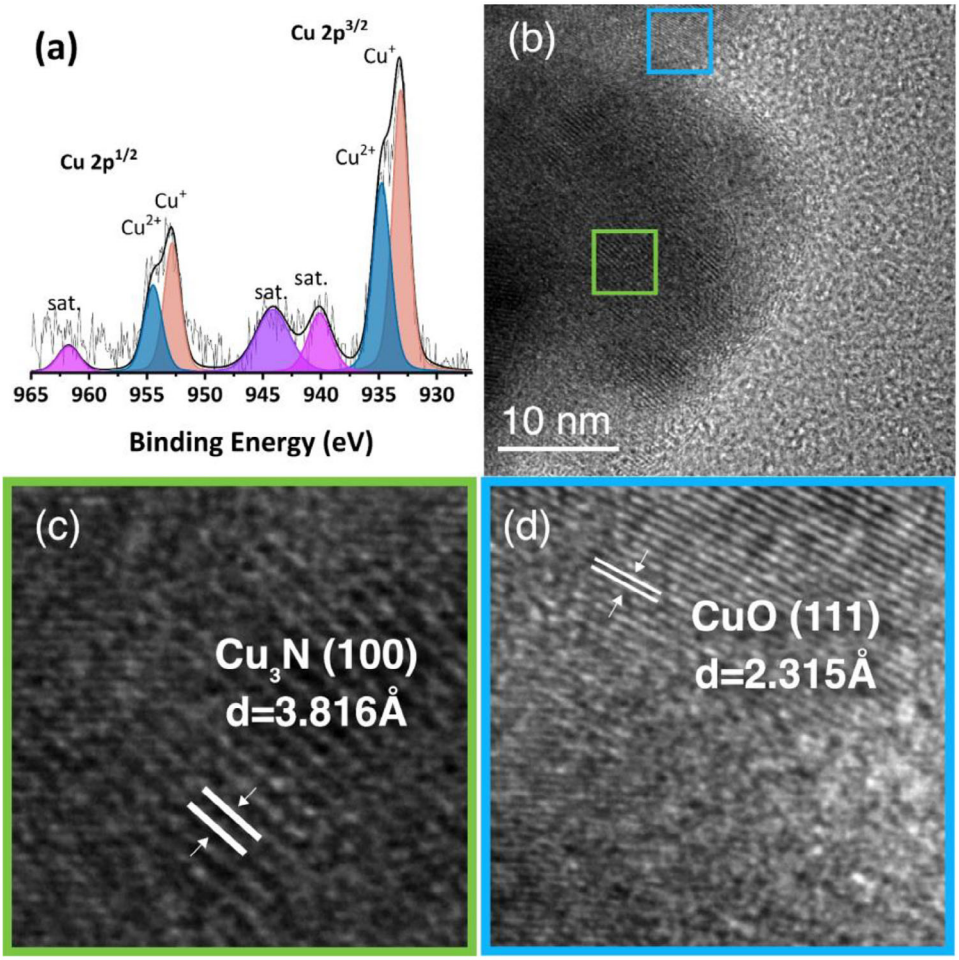

Figure 5. Characterization of Cu_3N catalyst after 10 C chronoamperometry at −0.9 V versus RHE: (a) Cu 2p XPS spectra, (b) high-resolution TEM image, (c) magnified region of Cu_3N (1 0 0) plane, and (d) magnified region of CuO (1 1 1) plane.

−0.9 V (Figure S16). However, this value is still three times lower than that achieved with Cu_3N, highlighting the superior catalytic activity of Cu_3N/CuO compared to CuO alone. The Cu_3N/CuO interface plays a crucial role in promoting NO_3RR activity. This observation correlates with literature reports on copper oxide nanostructures, which generally face limitations as electrocatalysts due to their low electrical conductivity, restricting their practical use.[14]

In light of the encouraging results obtained with Cu_3N, we evaluated the catalytic activity and selectivity of Cu_3P. Figure 6a compares the electrocatalytic performance of Cu_3P and Cu_3N catalysts for NO_3RR (solid lines) and for alkaline HER (dashed lines). Clearly, among the catalysts, Cu_3P proved to be the most active toward the competitive HER, exhibiting the lowest onset overpotential. DFT calculations show near-optimal ΔG_{H^*} values of Cu_3P sites, that is, allowing hydrogen to bind neither strong nor weak.[28] For Cu_3P, the addition of NO_3^- into the solution yielded an enhanced current density in a limited region up to −0.5 V (versus RHE), after which a clear transition to the HER regime is evident. At −0.5 V_{RHE}, the major product detected is nitrite, with FE of 66% and NH_3 yield rate of 10.5 mmol h^{-1} $mmol_{cat}$, but at higher potentials, the HER becomes dominant and the FE of nitrite declines rapidly, reaching less than 20% (NO_2^- + NH_3) at −0.9 V_{RHE} (Figure 6b,c). To further examine hydrogen evolution, a qualitative gas chromatography (GC) analysis was performed, confirming the presence of H_2 at higher potentials (Figure S17). The summarized electrochemical performance of all catalysts is available in Table S4. Another factor to consider is the electrochemical active surface areas (ECSA), which were evaluated by the electrochemical double-layer capacitances, as shown in Figure S18a–c. Cu_3N demonstrated almost 7 times as high ECSA as that of Cu_3P, which can promote the nitrate conversion rate. Structural characterization of the Cu_3P catalyst before and after NO_3RR showed that the Cu_3P nanoparticles retained their round shape and remained unaffected by electrocatalysis, as confirmed by HRTEM analysis (Figure S19a). Additionally, no significant oxide phase was detected, and the presence of the Cu_3P (300) plane in Figure S19b further supports the structural stability of the catalyst. Additionally, the XPS spectra revealed that the copper species were reduced during the electrocatalysis due to the removal of surface contamination, as indicated by the appearance of a distinct Cu^+ peak (see Figures S20 and S21 and a detailed peak list in Table S5).

The initial reduction of nitrate toward nitrite is a three-step electrochemical-chemical-electrochemical (ECE) mechanism as

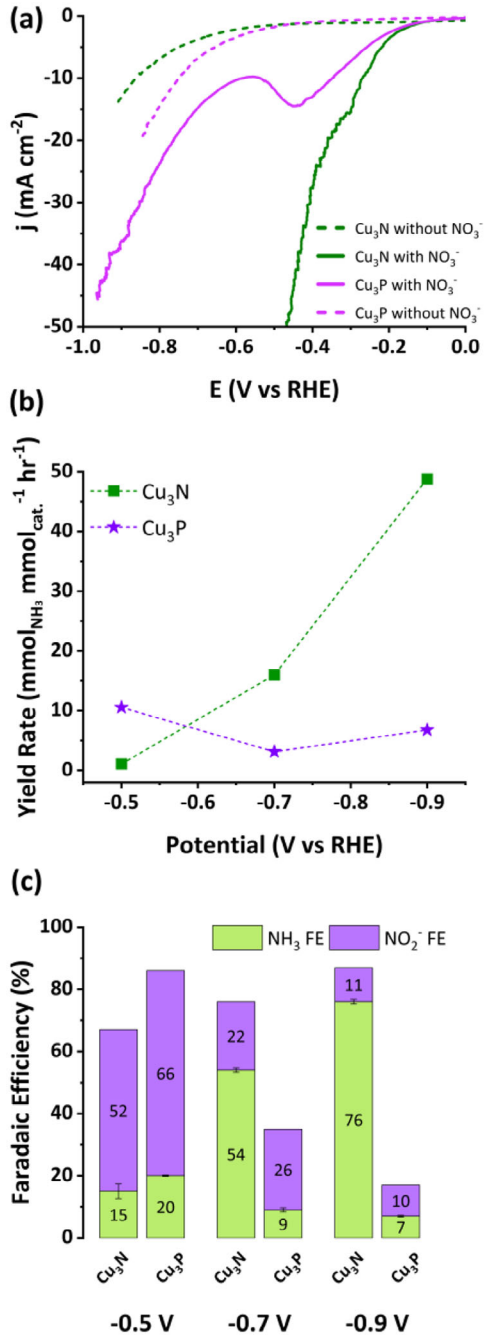

Figure 6. Electrochemical NO_3RR performances of Cu_3N and Cu_3P. (a) LSV scans in 0.1 M PBS, with and without 0.1 M $NaNO_3$. (b) NH_3 yield rates and (c) FEs of Cu_3P and Cu_3N at different given potentials. All potentials are iR-corrected.

described in Reactions (1)–(3).[29]

$$NO_3^-{}_{ads} + e^- \rightarrow NO_3^{2-}{}_{ads}\ (\text{limiting step}) \quad (1)$$

$$NO_3^{2-}{}_{ads} + H_2O \rightarrow NO_2{\cdot}_{ads} + 2OH^- \quad (2)$$

$$NO_2{\cdot}_{ads} + e^- \rightarrow NO_2^-{}_{ads} \longrightarrow NO_2^-{}_{aq} \quad (3)$$

The results demonstrate the importance of properly balancing the surface coverage of nitrate and hydrogen. The adsorbed *H is considered a key intermediate for nitrate hydrogenation, where the promotion of the first Volmer step (Reaction 4) and inhibition of the Tafel (Reaction 5) or Heyrovsky (Reaction 6) steps are desired.

$$H^+ (/H_2O) + e^- \rightarrow {}^*H_{ads}$$

(Volmer step; H_2O is the proton donor in non-acidic pH) (4)

$${}^*H + {}^*H \rightarrow H_2\ (\text{Tafel}) \quad (5)$$

$${}^*H + H^+ + e^- + \rightarrow H_2\ (\text{Heyrovsky}) \quad (6)$$

$$NO_2^-{}_{ads} + *H_{ads} \rightarrow OH^- + NO_{ads} \overset{Hads}{\rightarrow} \cdots .NH_3 \quad (7)$$

At less negative potentials, the hydrogen surface coverage is low due to high overpotential in neutral media. As a result, nitrite was the main product of the nitrate reduction, consistent with previous reports showing that Cu (I) species (existing on the surface of both catalysts) are predominant in the potential region where two-electron reduction of NO_3^- to NO_2^- is the major reaction.[30] As the potential is shifted cathodically (more negative), the Cu_3P surface is rapidly covered with *H compared to Cu_3N; therefore, the coupling of hydrogen atoms to form molecular hydrogen is faster than the hydrogenation of N-intermediates, leading to preferential hydrogen production. This overall picture suggests a cooperative mechanism of the NO_3RR in the heterogenous Cu_3N/CuO interface. The presence of oxophilic sites, such as copper (II) oxide,[31] acts as promoters for the water dissociation step to facilitate the formation of stable H_{ads} (Reaction 4), which in turn hydrogenates the adsorbed $NO_{2(ads)}$ formed at the nearby Cu (I) sites, ultimately producing NH_3 through consecutive reactions (Reaction 7). Recent studies show that balancing the production of *H and its consumption plays a key role in the efficient electrochemical conversion of NO_3^- to NH_3.[8,32] Extensive research is currently focused on designing non-noble nanomaterials for NO_3RR, with copper nitride-based catalysts only recently being investigated for the electrochemical reduction of nitrate to ammonia. A study on Cu_3(Pd)N nanocrystals, synthesized via a modified colloidal route with activated carbon, demonstrated an ammonia Faradaic efficiency (FE) of 77.3%, comparable to the 76.5% FE achieved by our Cu_3N catalyst.[13] However, the Cu_3PdN exhibited an ammonia yield rate approximately half that of our Cu_3N/CuO catalysts. Additionally, the high cost of palladium makes Cu_3PdN less attractive for practical applications than Cu_3N-based catalysts. The detailed comparison with recently reported electrocatalysts for NO_3^-RR is provided at Table S6.

4. Conclusions

Binary compounds consisting of Cu(I) and moderately electronegative elements are interesting and non-precious semiconductors for various applications. In this study, we demonstrate that a Cu_3N catalyst exhibits exceptional performance in the electrochemical reduction of nitrate to ammonia (NO_3RR),

achieving high Faradaic efficiency and yield rates. The formation of a Cu_3N/CuO interface during catalysis plays a crucial role in its activity, facilitating efficient NO_3RR through a stepwise reduction mechanism, with NO_2^- serving as a key intermediate. This performance significantly outpaces that of Cu_3P (and CuO) in NO_3RR activity and selectivity. The results indicate that this intriguing NO_3RR behavior is attributed to the synergistic effect of the cooperative Cu_3N/CuO interface with a conductive core. The cleavage of H_2O is favored to occur on the oxophilic oxide to form stable H_{ads}, thus creating a strong reducing environment for catalytic hydrogenation of the nitrogen intermediate species formed at the nearby Cu(I) sites, ultimately producing NH_3. On the other hand, our findings indicate that although Cu_3P is effective in the initial reduction of nitrate to nitrite, it fails to produce NH_3 at more negative potentials due to competition with the hydrogen evolution reaction (HER). This work paves the way for designing non-precious metal-based cooperative electrocatalysts for NO_3RR, highlighting the delicate balancing of H* and $*NO_3$ intermediate adsorption to enhance NO_3RR efficiency.

Supporting Information

The following files are available free of charge.

An extended materials and methods section, SEM images, calculation of lattice parameters, XPS binding energy tables, XPS data for O, N, P, performance of Cu_3N catalysts in various nitrate concentration, optimization of the Cu_3N synthesis protocols, calibration curves for the determination of the products concentrations by a colorimetric technique and by NMR, characterization of the catalysts after the catalytic measurements.

Author Contributions

The manuscript was written through contributions of all authors. All authors have given approval to the final version of the manuscript.

Acknowledgements

This research was supported by the Israeli Atomic Energy Commission-Prof. A. Pazy joint foundation (ID126-2020) and the Israel Science Foundation (Grant No. 650/21).

Conflict of Interests

The authors declare no conflict of interest.

Data Availability Statement

The data that support the findings of this study are available from the corresponding author upon reasonable request.

Keywords: Ammonia · Copper-based nanocatalysts · Electrocatalysis · Nitrate reduction · NO_3RR

[1] F. Jiao, B. Xu, *Adv. Mater.* **2019**, *31*, 1805173.
[2] W. Chen, X. Yang, Z. Chen, Z. Ou, J. Hu, Y. Xu, Y. Li, X. Ren, S. Ye, J. Qiu, J. Liu, Q. Zhang, *Adv. Funct. Mater.* **2023**, *33*, 2300512.
[3] Y. Xiong, Y. Wang, J. Zhou, F. Liu, F. Hao, Z. Fan, *Adv. Mater.* **2023**, *36*, 2304021.
[4] J. D. Genders, D. Hartsough, D. T. Hobbs, *J. Appl. Electrochem.* **1996**, *26*, 1–9.
[5] Z. Zhang, N. Zhang, J. Zhang, B. Deng, Z. Cao, Z. Wang, G. Wei, Q. Zhang, R. Jia, P. Xiang, *Chem. Eng. J.* **2024**, *483*, 148952.
[6] H. Xu, Y. Ma, J. Chen, W.-X. Zhang, J. Yang, *Chem. Soc. Rev.* **2022**, *51*, 2710–2758.
[7] Z. Wang, D. Richards, N. Singh, *Catal. Sci. Technol.* **2021**, *11*, 705–725.
[8] K. Fan, W. Xie, J. Li, Y. Sun, P. Xu, Y. Tang, Z. Li, M. Shao, *Nat. Commun.* **2022**, *13*, 7958.
[9] K. Xu, P. Chen, X. Li, Y. Tong, H. Ding, X. Wu, W. Chu, Z. Peng, C. Wu, Y. Xie, *J. Am. Chem. Soc.* **2015**, *137*, 4119–4125.
[10] P. De Luna, R. Quintero-Bermudez, C.-T. Dinh, M. B. Ross, O. S. Bushuyev, P. Todorović, T. Regier, S. O. Kelley, P. Yang, E. H. Sargent, *Nat. Catal.* **2018**, *1*, 103–110.
[11] Z. Gong, X. Xiang, W. Zhong, C. Jia, P. Chen, N. Zhang, S. Zhao, W. Liu, Y. Chen, Z. Lin, *Angew. Chem., Int. Ed.* **2023**, *135*, e202308775.
[12] B. Zhang, Z. Dai, Y. Chen, M. Cheng, H. Zhang, P. Feng, B. Ke, Y. Zhang, G. Zhang, *Nat. Commun.* **2024**, *15*, 2816.
[13] K. Yao, Z. Fang, J. Wang, W. Wang, M. Wang, W. Yan, M. Ye, B. Jiang, K. Wu, X. Wei, *Chem. Commun.* **2023**, *59*, 12176–12179.
[14] Z. Du, K. Yang, H. Du, B. Li, K. Wang, S. He, T. Wang, W. Ai, *ACS Appl. Mater. Interfaces* **2023**, *15*, 5172–5179.
[15] Y. Wang, A. Xu, Z. Wang, L. Huang, J. Li, F. Li, J. Wicks, M. Luo, D.-H. Nam, C.-S. Tan, *J. Am. Chem. Soc.* **2020**, *142*, 5702–5708.
[16] Y. Wang, W. Zhou, R. Jia, Y. Yu, B. Zhang, *Angew Chem. Int. Ed.* **2020**, *59*, 5350–5354.
[17] X. F. Cheng, J. H. He, H. Q. Ji, H. Y. Zhang, Q. Cao, W. J. Sun, C. L. Yan, J. M. Lu, *Adv. Mater.* **2022**, *34*, 2205767.
[18] A. Sajeev, A. M. Paul, R. Nivetha, K. Gothandapani, T. S. Gopal, G. Jacob, M. Muthuramamoorty, S. Pandiaraj, A. Alodhayb, S. Y. Kim, *Sci. Rep.* **2022**, *12*, 2004.
[19] D. Bandyopadhyay, S. Ghosh, L. Houben, R. Bar-Ziv, M. Bar-Sadan, *ACS Appl. Energy Mater.* **2023**, *6*, 10987–10995.
[20] X. Li, J. Zhang, Y. Zhang, R. Zhang, D. Chen, C. Zhang, X. Zhang, B. Wang, H. Q. Luo, N. B. Li, *Int. J. Hydrogen Energy* **2020**, *45*, 21422–21430.
[21] Z. Yin, C. Yu, Z. Zhao, X. Guo, M. Shen, N. Li, M. Muzzio, J. Li, H. Liu, H. Lin, *Nano Lett.* **2019**, *19*, 8658–8663.
[22] S. Wei, K. Qi, Z. Jin, J. Cao, W. Zheng, H. Chen, X. Cui, *ACS Omega* **2016**, *1*, 1367–1373.
[23] J. Wei, G. Ye, H. Lin, Z. Li, J. Zhou, Y.-Y. Li, *J. Colloid Interface Sci.* **2024**, *670*, 798-807.
[24] M. Parvizian, A. Duràn Balsa, R. Pokratath, C. Kalha, S. Lee, D. Van den Eynden, M. Ibáñez, A. Regoutz, J. De Roo, *Angew. Chem., Int. Ed.* **2022**, *61*, e202207013.
[25] L. S. Clesceri, A. E. Greenberg, A. D. Eaton, *Standard Methods for the Examination of Water and Wastewater*, 20th ed., APHA American Public Health Association, Washington DC **1998**.
[26] Y. Wang, C. Wang, M. Li, Y. Yu, B. Zhang, *Chem. Soc. Rev.* **2021**, *50*, 6720–6733.
[27] S. Z. Andersen, V. Čolić, S. Yang, J. A. Schwalbe, A. C. Nielander, J. M. McEnaney, K. Enemark-Rasmussen, J. G. Baker, A. R. Singh, B. A. Rohr, *Nature* **2019**, *570*, 504–508.
[28] Z. Zhang, G. Yu, H. Li, J. Liu, X. Huang, W. Chen, *Phys. Chem. Chem. Phys.* **2018**, *20*, 10407–10417.
[29] Z. Zhang, N. Zhang, J. Zhang, B. Deng, Z. Cao, Z. Wang, G. Wei, Q. Zhang, R. Jia, P. Xiang, *Chem. Eng. J.* **2024**, *483*, 148952.
[30] L. Bai, F. Franco, J. Timoshenko, C. Rettenmaier, F. Scholten, H. S. Jeon, A. Yoon, M. Rüscher, A. Herzog, F. T. Haase, *J. Am. Chem. Soc.* **2024**, *146*, 9665–9678.

[31] T. V. Vineesh, V. Yarmiayev, D. Zitoun, *Electrochem. Commun.* **2020**, *113*, 106691.
[32] J. Yu, R. T. Gao, X. Guo, N. Truong Nguyen, L. Wu, L. Wang, *Angew. Chem., Int. Ed.* **2025**, *64*, e202415975.

Manuscript received: February 17, 2025
Accepted manuscript online: February 23, 2025
Version of record online: ■■, ■■